

CONTENTS

1	SED PROPERTIES	1
1.1	Data	1
1.1.1	The Sloan Digital Sky Survey	2
1.1.2	UKIDSS Large Area Survey	2
1.1.3	WISE All-WISE Survey	2
1.1.4	Completeness of Photometry	3
1.1.5	Final Sample	3
1.2	SED Model	3
1.2.1	Accretion Disk	3
1.2.2	Hot Dust	5
1.2.3	Emission Lines	5
1.2.4	Host Galaxy	6
1.2.5	Lyman- α Forest Absorption	8
1.2.6	Lyman-Limit Systems	9
1.2.7	Dust Extinction	9
1.3	The ‘Standard’ SED Model	10
1.4	Discussion of Fit	11
1.4.1	Flux Correction	15
1.5	Hot Dust	15
1.5.1	Parameterising the hot dust emission	16
1.5.2	Sample	16
1.5.3	Diversity in hot dust properties	18
1.6	Fitting procedure	21
1.7	Results	23
1.7.1	Correlations with quasar properties	23
1.7.2	Spectral properties	23
1.7.3	BALs and radio-loud/radio-quiet	25
1.8	Other works	27
1.8.1	Eddington ratio	28

LIST OF FIGURES

- Figure 1.1 Model spectrum at $z = 1$, showing the contributions to the total flux from the blue power-law slope, red power-law slope, blackbody and host galaxy. The locations of the most prominent emission lines in the spectrum are also indicated. [4](#)
- Figure 1.2 Model spectrum at three different redshifts (each arbitrarily scaled), and throughput functions for SDSS, UKIDSS and WISE band-passes (scaled so that the peak transmission is equal to one.) The dashed line indicates the slope of the AB magnitude system zero point. [10](#)
- Figure 1.3 Colours of median SED (*black circles*), individual objects (*grey points*), best-fitting model (*black line*) as a function of redshift. [12](#)
- Figure 1.4 Colours of median SED (*black circles*), individual objects (*grey points*), best-fitting model (*black line*) as a function of redshift. [13](#)
- Figure 1.5 Residuals from fit to DR7Q-matched catalogue as a function of rest-frame wavelength. [14](#)
- Figure 1.6 Ratio of NIR to UV luminosity ($R_{\text{NIR/UV}}$) against temperature (T_{BB}) for low- z sample. The density of points is shown in more dense regions of the space, and individual objects in less dense regions. [17](#)

- Figure 1.7 $i - K$ vs z . Demonstrates how sample was defined. The grey points show, as a function of redshift, the $i - K$ colours of all DR7Q quasars which are not classified as broad-absorption line quasars by Shen et al. and i magnitude > 19.1 . The black line shows the $i - K$ colour of our standard, unreddened SED model as a function of redshift. The red and blue lines show the $i - K$ colours of our SED model with dust reddening $E(B-V) = 0.075$ and $E(B-V) = -0.075$ respectively. A significant amount of this reddening can be attributed to intrinsic variations in the UV power-law slopes of the individual quasars, which is why we allow a negative reddening. However, there is a clear 'red tail' to the colour distribution which can be explained by dust reddening at the redshift of the quasar. We defined two samples, at low ($0.5 < z < 1.5$) and high ($2 < z < 2.7$) redshift, which are shown in the figure. 19
- Figure 1.8 $W1 - W2$ colours of DR7 sample as a function of redshift. Above a certain density threshold points are represented by a density plot. On top we plot the colours of our standard SED model, with a fixed temperature and a varying NIR ($1 - 3 \mu\text{m}$) to UV ratio. 20
- Figure 1.9 Ratio of NIR to UV luminosity ($R_{\text{NIR/UV}}$) against temperature (T_{BB}). The grey contours show equally-spaced lines of constant probability density generated using a Gaussian kernel-density estimator on our data sample. The black points are for our mock data. 21
- Figure 1.10 Best-fit black-body temperature against UV luminosity (left), black-hole mass (center) and Eddington ratio (right) for $1 < z < 1.5$ sample (black) and $2 < z < 2.7$ sample (black). In region of high-density we represent the density with contours generated using a Gaussian kernel density estimation. Needs re-making with new BH masses. 22
- Figure 1.11 Composite SDSS spectra for objects at $z \sim 0.7$. We have divided sample into objects with objects best-fit by small (red line) and large (red line) values of β . Change this to select by $R_{\text{NIR/UV}} / T_{\text{BB}}$. Label prominent emission lines. 24

Figure 1.12	Rest-frame equivalent width and blueshift of the C IV line for 7,115 SDSS DR7 quasars. The colours of the hexagons denote the median hot dust ($T \simeq 1200$ K) abundance for all quasars at a given equivalent width and blueshift. Quasars with the most extreme outflow signatures are predominantly hot-dust rich. Only bins containing a minimum of two objects are plotted.	25
Figure 1.13		26
Figure 1.14		26

LIST OF TABLES

Table 1.1	Best-fitting parameters from fit to DR7Q-matched sample. Only give best-fit values after correction.	14
-----------	---	----

LISTINGS

ACRONYMS

SED PROPERTIES

At the start, there are various different ways one could "motivate" the investigation but you could develop your initial starting point [lots of new data now available for 10s of thousands of quasars that covers significant range in luminosity, redshift, and rest-frame wavelength] in the context of your new BH masses - asking whether there are SED-related systematics as a function of "outflow" signatures and BH mass? Would give you a story of looking for additional information even if it turns out that there isn't anything stunning . Also fairly naturally give you a "further work and/or what more is needed to test model(s)?" link.

While many authors have focused on studies of specific sub-sets of active galactic nuclei (AGN) with extreme observational properties, what is missing is an understanding of how these extreme subsets relate to the population as a whole. I have addressed this problem using multi-wavelength spectral energy distributions (SEDs) of large samples of quasars. I have constructed an SED model which is able to reproduce the average optical to near-infrared (NIR) colours of 10,000s of AGNs spanning a broad range in redshift and luminosity.

Irrespective of how the motivation at the start is written, think you definitely need an orientation sub-section that gets across to the reader what signatures [of physical components/processes associated with the quasar central regions] you can probe given the rest-frame wavelength range. Also outline "complications", e.g. host galaxies, reddening,... so that the reader is prepared for the different selection criteria, flux limits,... introduced later.

Perhaps also say something about how not very thoughtful generation of "composite" spectra (with huge quasar luminosity range as a function of wavelength and also presence of significant host galaxy at optical wavelengths from low-z objects) has confused situation and use as a rationale for your parametric model approach?

1.1 DATA

The systematic study of the dependence of the SED shape on physical parameters has, until very recently, been limited by the difficulty in obtaining a large sample of quasars with good multi-wavelength coverage and large dynamic range in luminosity and redshift. In this work, we take advantage of a number of recent, sensitive, wide-field surveys, covering the UV to mid-IR spectral region.

1.1.1 The Sloan Digital Sky Survey

We use the Seventh Data Release (DR7) of the Sloan Digital Sky Survey (SDSS; York et al., 2000) spectroscopic quasar catalogue (Schneider et al., 2010), which includes 105,783 objects across 9380 deg². The SDSS obtained images in five broad optical passbands: u ($\lambda_{\text{eff}} = 3543\text{\AA}$), g ($\lambda_{\text{eff}} = 4770\text{\AA}$), r ($\lambda_{\text{eff}} = 6231\text{\AA}$), i ($\lambda_{\text{eff}} = 7625\text{\AA}$), and z ($\lambda_{\text{eff}} = 9134\text{\AA}$). We use BEST point-spread function (PSF) magnitudes, correcting for Galactic extinction using the maps of Schlegel, Finkbeiner, and Davis, (1998), assuming a Milky Way (MW) extinction curve (Pei, 1992) and an extinction to reddening ratio $A(V)/E(B - V) = 3.1$. Although the SDSS asinh magnitude system is intended to be on the AB system (Oke and Gunn, 1983), the photometric zero-points are known to be slightly off the AB standard. To account for this we add 0.03 mag to the u, g, r and i magnitudes, and 0.05 mag to the z magnitude.

Where did these numbers come from?

DR7Q quasar targets were primarily selected to have $i \leq 19.1$ if the colours were consistent with being at redshift $z < 3$, and $i \leq 20.2$ if consistent with $z > 3$ (Richards et al., 2002). The survey is sensitive to the most luminous quasars at a given redshift. The large number of objects at $z < 3$ with $i > 19.1$ were selected by algorithms other than the main quasar selection. For example, quasar targets were also selected if they matched within $2''$ of an object in the Faint Images of the Radio Sky at Twenty-cm (FIRST) catalogue of radio sources (Becker, White, and Helfand, 1995).

1.1.2 UKIDSS Large Area Survey

We use the UKIRT Infrared Deep Sky Survey (UKIDSS; Lawrence et al., 2007) Large Area Survey (ULAS) which has observed $\sim 3,200$ deg² in four near-IR passbands: Y ($\lambda_{\text{eff}} = 1.0305\mu\text{m}$), J ($\lambda_{\text{eff}} = 1.2483\mu\text{m}$), H ($\lambda_{\text{eff}} = 1.6313\mu\text{m}$), and K ($\lambda_{\text{eff}} = 2.2010\mu\text{m}$). We used the ninth data release (DR9) of the ULAS. Cross-matching (with a $2''$ radius and picking only the nearest neighbour) the SDSS DR7Q catalogue with the ULAS catalogue, which covers only $\sim 38\%$ of the SDSS footprint, resulted in 37,893 matches. The ULAS magnitudes are aperture corrected magnitudes in a $2''$ diameter aperture and are not corrected for Galactic extinction.

1.1.3 WISE All-WISE Survey

The Wide-field Infrared Explorer (WISE; Wright et al., 2010) mapped almost the sky in four mid-IR band-passes: W1 ($\lambda_{\text{eff}} = 3.4\mu\text{m}$), W2 ($\lambda_{\text{eff}} = 4.6\mu\text{m}$), W3 ($\lambda_{\text{eff}} = 12\mu\text{m}$), and W4 ($\lambda_{\text{eff}} = 22\mu\text{m}$). The WISE AllWISE Data Release ('AllWISE') combines data from the nine month cryogenic phase of the mission that led to the 'AllSky' data

release with data from the NEOWISE program (Mainzer et al., 2011). Cross-referencing the SDSS DR7Q catalogue with the AllWISE catalogue resulted in 102,734 matches. Two objects were matched to multiple AllWISE objects, and were discarded from the sample. Vega to AB conversion factors for WISE photometry are given in the WISE Explanatory Supplement (Cutri et al., 2013)

1.1.4 Completeness of Photometry

Objects which are faint in the SDSS *i* band-passes are more likely to have magnitudes which fall below the limiting magnitudes of the UKIDSS and WISE band-passes at longer wavelengths. For a given *i* magnitude, a quasar with a blue spectrum is more likely to be undetected at longer wavelengths than a quasar with a red spectrum. Therefore, as we allow fainter quasars in to our sample we will be biased towards objects with redder spectra. We impose an observed *i* magnitude lower limit of 19.1 mag, which is the magnitude limit of the main SDSS colour-selection algorithm. We verified that above this limit the DR7Q-matched sample is 95% complete in all band-passes with $S/N > 5$ (excluding WISE W3 and W4) and that this fraction is not changing rapidly with the brightness of the sample.

1.1.5 Final Sample

We exclude objects flagged as BALQSOs by Shen et al., (2011), since our model is unable to reproduce the broad absorption troughs that appear in the spectra of these objects. The final sample contains 61,411 objects in the redshift range $0.2 < z < 3.8$.

1.2 SED MODEL

I have constructed a new SED model which reproduces the SEDs of AGNs from the rest-frame UV ($\sim 0.1\mu\text{m}$) to the rest-frame near-IR ($\sim 3\mu\text{m}$). In this section, I will describe how I have modelled the emission from the various components contributing to the emission in this spectral region. The model spectrum is shown in Figure 1.1, with each of the main components indicated.

1.2.1 Accretion Disk

More than half the bolometric luminosity of an unobscured AGN is emitted in the Big Blue Bump, which extends from the near-IR at $1\mu\text{m}$ to past $0.1\mu\text{m}$ in the UV, and possibly all the way to the soft X-ray region. The Big Blue Bump emission is thought to arise from an accretion disc. In the $0.1 - 1\mu\text{m}$ region the spectrum is generally

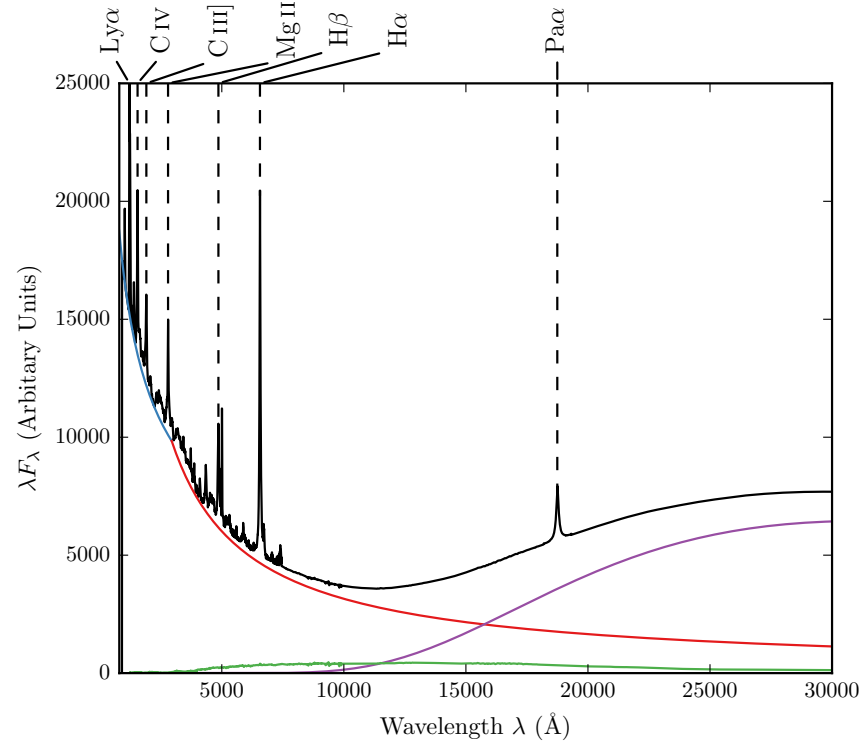


Figure 1.1: Model spectrum at $z = 1$, showing the contributions to the total flux from the blue power-law slope, red power-law slope, black-body and host galaxy. The locations of the most prominent emission lines in the spectrum are also indicated.

characterised by a power-law of the form $F_\nu = C\nu^{-\alpha}$ where α is the power-law index, C is a constant, and F_ν is the flux per unit frequency, usually measured in units of $\text{erg s}^{-1} \text{cm}^{-2} \text{Hz}^{-1}$. Equivalently this can be expressed as $F_\lambda = C'\lambda^{\alpha-2}$ where F_λ is the flux per unit wavelength, usually measured in units of $\text{s}^{-1} \text{cm}^{-2} \text{\AA}^{-1}$.

The value of the power-law index is uncertain. From a theoretical perspective, models of geometrically thin accretion discs (Shakura and Sunyaev, 1973) assume, in particular, that the disc is stationary, axisymmetric, and extends down to the innermost stable circular orbit, and that angular momentum is transported by local ‘viscous’ stresses that convert gravitational energy entirely into heat. This gives the dependence of the effective temperature on radius as $t_{\text{eff}} \propto r^{-3/4}$. A spectrum is then calculated by dividing the disc into concentric annuli, calculating the spectrum emitted by each annulus and then summing them all together. Assuming that each annulus radiates like a blackbody, the $r^{-3/4}$ effective temperature distribution gives $F_\nu \propto \nu^{1/3}$ (Peterson, 1997), although it is unclear whether this is consistent with observations.

In our model we characterised the Big Blue Bump from $\sim 0.1 - 1\mu\text{m}$ as a broken power-law with three free parameters: a break-wavelength λ_{break} , a blue power-law index α_{blue} for wavelengths shorter than the break wavelength, and a red power-law index α_{red} for wavelengths longer than the break wavelength.

1.2.2 Hot Dust

At wavelengths longer than $1\mu\text{m}$, emission from hot dust begins to dominate over emission from the accretion disc. The SED in this region is generally characterised either by a power-law ($\propto \lambda^{\beta_{\text{NIR}}}$), with $\beta \simeq 0.5$ (e.g. Richards et al., 2006; Zhang et al., 2014), or by a blackbody at $\sim 1300 \text{ K}$, thus peaking in the near-IR (e.g. Leipski et al., 2014). We modelled the hot dust emission using a simple blackbody:

$$F_\lambda = \frac{2hc^2}{\lambda^5} \frac{1}{e^{\frac{hc}{\lambda k_B T}} - 1} \quad (1.1)$$

The blackbody component has two free parameters: the temperature of the blackbody T_{BB} and the overall normalisation.

1.2.3 Emission Lines

Hundreds of emission lines are present in a typical AGN spectra. Some of the most prominent lines are shown in Figure 1.1. The emission line spectrum is taken from Maddox and Hewett, (2006), who extend the composite of Francis et al., (1991) to include the $\text{H}\alpha$ (6560\AA)

and $\text{Pa}\alpha$ (18750\AA) emission lines. A single parameter, EL_{scale} , scales the equivalent widths of all emission lines equally:

$$F_{\lambda} = \text{EL}_{\text{scale}} \times \frac{F_{\lambda,\text{el}}}{F_{\lambda,\text{cont}}} \times F_{\lambda} \quad (1.2)$$

where $F_{\lambda,\text{el}}$ is the line flux in the template, $F_{\lambda,\text{cont}}$ is the continuum flux in the template, and F_{λ} is the continuum flux in the model.

1.2.4 Host Galaxy

Emission from the host galaxy is important, particularly in the region around the $1\mu\text{m}$ inflection point in the quasar SED. While the host galaxies of bright quasars tend to be massive, bright ellipticals, the hosts of lower luminosity AGN can have disc components (e.g. Dunlop et al., 2003). Our model incorporates $z = 0$ Sa, Sb, Sc and elliptical-type templates from Mannucci et al., (2001), which for simplicity do not evolve with redshift. We characterise the relationship between the luminosity of the AGN L_{AGN} and the luminosity of the host galaxy L_{Gal} as a power-law

$$L_{\text{Gal}} = L_{\text{AGN}}^{\beta} \quad (1.3)$$

with power-law index $\beta = 0.42$ (Maddox and Hewett, 2006). Dividing both sides of Equations 1.3 by the luminosity of the AGN gives the luminosity of the host galaxy relative to the luminosity of the AGN

$$\frac{L_{\text{Gal}}}{L_{\text{AGN}}} = L_{\text{AGN}}^{\beta-1} \quad (1.4)$$

which for $\beta < 1$ decreases with increasing AGN luminosity. In a flux limited sample, the AGN luminosity will tend to increase with redshift and so the luminosity of the host galaxy relative to the luminosity of the quasar will decrease with increasing redshift. Hence, the contribution from the host galaxy to the total flux is important at low redshift, but becomes gradually less significant towards higher redshifts.

Since the contribution from the host galaxy to the flux changes as a function of AGN luminosity, and hence redshift, we choose a reference redshift z_{norm} where we set the fractional contribution of the host galaxy to the total flux, η . In an arbitrary region of the spectrum (we use $4000 - 5000 \text{\AA}$) we calculate both the AGN continuum flux $F_{\text{AGN}}(z_{\text{norm}})$ and the flux from our host galaxy template spectrum $F_{\text{Gal}}(z_{\text{norm}})$. The fractional contribution from the host galaxy to the total flux is then:

$$\eta = \frac{CF_{\text{Gal}}(z_{\text{nrn}})}{F_{\text{AGN}}(z_{\text{nrn}}) + CF_{\text{Gal}}(z_{\text{nrn}})} \quad (1.5)$$

where the constant C is the factor by which we must multiply the unnormalised galaxy spectrum in order for Equation 1.5 to hold true. Rearranging for the constant C we find

$$C = \frac{\eta}{1 - \eta} \frac{F_{\text{AGN}}(z_{\text{nrn}})}{F_{\text{Gal}}(z_{\text{nrn}})} \quad (1.6)$$

Hence at redshift z_{nrn} the host galaxy flux we add to our rest frame quasar continuum is

$$F_{\lambda} = \frac{\eta}{1 - \eta} \frac{F_{\text{AGN}}(z_{\text{nrn}})}{F_{\text{Gal}}(z_{\text{nrn}})} F_{\lambda, \text{Gal}} \quad (1.7)$$

where $F_{\lambda, \text{Gal}}$ is our host galaxy template spectrum in the quasar rest frame. The contribution from the host galaxy at a different redshift z is given by

$$F_{\lambda} = \frac{\eta}{1 - \eta} \frac{F_{\text{AGN}}(z)}{F_{\text{Gal}}(z)} \frac{F_{\text{AGN}}(z_{\text{nrn}})}{F_{\text{Gal}}(z_{\text{nrn}})} \left(\frac{F_{\text{AGN}}(z)}{F_{\text{Gal}}(z)} \right)^{-1} F_{\lambda, \text{Gal}} \quad (1.8)$$

$$= \frac{\eta}{1 - \eta} \frac{F_{\text{AGN}}(z)}{F_{\text{Gal}}(z)} \frac{F_{\text{AGN}}(z_{\text{nrn}})}{F_{\text{Gal}}(z_{\text{nrn}})} \frac{F_{\text{Gal}}(z)}{F_{\text{AGN}}(z)} F_{\lambda, \text{Gal}} \quad (1.9)$$

$$= \frac{\eta}{1 - \eta} \frac{F_{\text{AGN}}(z)}{F_{\text{Gal}}(z)} \frac{L_{\text{AGN}}(z_{\text{nrn}})}{L_{\text{Gal}}(z_{\text{nrn}})} \frac{L_{\text{Gal}}(z)}{L_{\text{AGN}}(z)} F_{\lambda, \text{Gal}} \quad (1.10)$$

$$= \frac{\eta}{1 - \eta} \frac{F_{\text{AGN}}(z)}{F_{\text{Gal}}(z)} \frac{L_{\text{AGN}}(z_{\text{nrn}})}{L_{\text{AGN}}(z_{\text{nrn}})^{\beta}} \frac{L_{\text{AGN}}(z)^{\beta}}{L_{\text{AGN}}(z)} F_{\lambda, \text{Gal}} \quad (1.11)$$

$$= \frac{\eta}{1 - \eta} \frac{F_{\text{AGN}}(z)}{F_{\text{Gal}}(z)} \left(\frac{L_{\text{AGN}}(z)}{L_{\text{AGN}}(z_{\text{nrn}})} \right)^{\beta-1} F_{\lambda, \text{Gal}} \quad (1.12)$$

We need to know how the luminosity of the AGN depends on redshift. This is given by:

$$\frac{L_{\text{AGN}}(z)}{L_{\text{AGN}}(z_{\text{nrn}})} = 10^{-0.4(M_{\text{AGN}}(z) - M_{\text{AGN}}(z_{\text{nrn}}))} \quad (1.13)$$

where $M_{\text{AGN}}(z)$, the absolute magnitude of an AGN at redshift z , is given by

$$M(z) = m - 5(\log_{10} D_L(z) - 1) \quad (1.14)$$

and $D_L(z)$ is the luminosity distance to a source at redshift z in parsecs. Hence:

$$\frac{L_{\text{AGN}}(z)}{L_{\text{AGN}}(z_{\text{nrn}})} = 10^{-0.4(M_{\text{AGN}}(z) - M_{\text{AGN}}(z_{\text{nrn}}))} \quad (1.15)$$

$$= 10^{(\log_{10} \left(\frac{D_L(z)}{D_L(z_{\text{nrn}})} \right)^2)} \quad (1.16)$$

1.2.5 *Lyman- α Forest Absorption*

As Paul how he implements this. My code for this can easily be sped up.

The optical spectra of high redshift quasars show hundreds of sharp absorption lines, which mostly correspond to the redshifted neutral hydrogen Ly α 1216Å transition. These absorption features are collectively referred to as the *Lyman- α forest*. To simulate the effect of Lyman- α forest absorption on our model SED we use the parametrisation of Becker et al., (2013), who derived an analytic function for the effective optical depth τ_{eff} over the redshift range $2 < z < 5$ made using 6065 quasar spectra from SDSS DR7. In their model the effective optical depth τ_{eff} is given by

$$\tau_{\text{eff}} = \tau_0 \times \left(\left(\frac{1+z}{1+z_0} \right)^b + C \right) \quad (1.17)$$

where,

$$\begin{aligned} t_0 &= 0.751 \\ b &= 2.9 \\ C &= -0.132 \\ z_0 &= 3.5 \end{aligned}$$

The transmitted flux $F_{\lambda, \text{trans}}$ at redshift z is then given by

$$f_{\lambda, \text{trans}} = F_{\lambda} \times e^{-\tau_{\text{eff}}} \quad (1.18)$$

An absorption line at λ_{abs} in the rest-frame of an AGN at redshift z_{AGN} has wavelength

$$(1 + z_{\text{AGN}})\lambda_{\text{abs}} \quad (1.19)$$

in the rest frame of an observer on Earth. In the rest-frame of a cloud of neutral hydrogen at redshift z_{cloud} the absorption line has wavelength

$$\frac{(1 + z_{\text{AGN}})\lambda_{\text{abs}}}{(1 + z_{\text{cloud}})} \quad (1.20)$$

and so to absorb Lyman- α at 1216 Å the gas cloud must be at a redshift

$$z_{\text{cloud}} = \frac{(1 + z_{\text{AGN}})\lambda_{\text{abs}}}{1216\text{Å}} - 1 \quad (1.21)$$

For every wavelength $\lambda_{\text{abs}} < 1216 \text{ Å}$ in the rest-frame of an AGN at redshift $z > 2$ we calculate z_{cloud} using Equation 1.21 and then calculate the transmitted flux at λ_{abs} by substituting z_{cloud} in to Equations 1.17 and 1.18.

1.2.6 Lyman-Limit Systems

Lyman-limit systems are clouds of HI which are optically thick at the Lyman limit (912Å), which generally implies a neutral hydrogen column density $N(\text{HI}) > 10^{17} \text{cm}^{-2}$. Photons at wavelengths shorter than the Lyman-limit will be absorbed, which creates a sharp break in the observed continuum. We model the effect of a Lyman-limit system at the redshift of the quasar by setting the flux at wavelengths less than 912Å in the quasar rest frame to zero.

Ask Paul if this should be implemented

1.2.7 Dust Extinction

The selection criteria of the SDSS DR7Q catalogue, and particularly the DR10Q catalogue, are sensitive to quasars with moderate amounts of dust reddening (possibly as high as $E(B-V) \sim 0.5$; Richards et al., 2003) at the redshift of the quasar, and so we included the effect of dust extinction in our model. We considered four types of extinction curve: the Large Magellanic Cloud (LMC), Small Magellanic Cloud (SMC), Milky-Way (MW) extinction curves from Pei, (1992) and an extinction curve appropriate for the quasar population which has been derived by Paul Hewett. To derive the quasar extinction curve, UKIDSS photometry was used to provide an $E(B-V)$ estimate, via the magnitude displacement of each quasar from the locus of unreddened objects. At redshifts $2 < z < 3$ the reddening measure is made at rest-frame wavelengths 3500-7000Å, where Galaxy, LMC and SMC extinction curves are very similar. The SDSS spectra of the same objects are then employed to generate an empirical extinction curve in the ultraviolet, down to 1200Å. The resulting curve has no 2200Å feature and rises rapidly with decreasing wavelength but is not as steep as the SMC curve. The extinction curves give the colour excess $E(B - \lambda)$ relative to the colour excess $E(B - V)$ as a function of wavelength λ . The colour excess $E(B - V)$ is related to the extinction in the V band, $A(V)$, via a parameter R ,

$$A(V) = R \times E(B - V) \quad (1.22)$$

where $R = 3.1$ in the MW and $R \simeq 3$ in the Magellanic Clouds. Hence the extinction at a wavelength λ $A(\lambda)$ is

$$A(\lambda) = E(B - V) \times \left[\frac{E(\lambda - V)}{E(B - V)} + R \right] \quad (1.23)$$

where the colour excess $E(B - V)$ is a free parameter in our model. The attenuation of the flux at a given wavelength is then:

$$F_\lambda = F_\lambda 10^{-A(\lambda)/2.5} \quad (1.24)$$

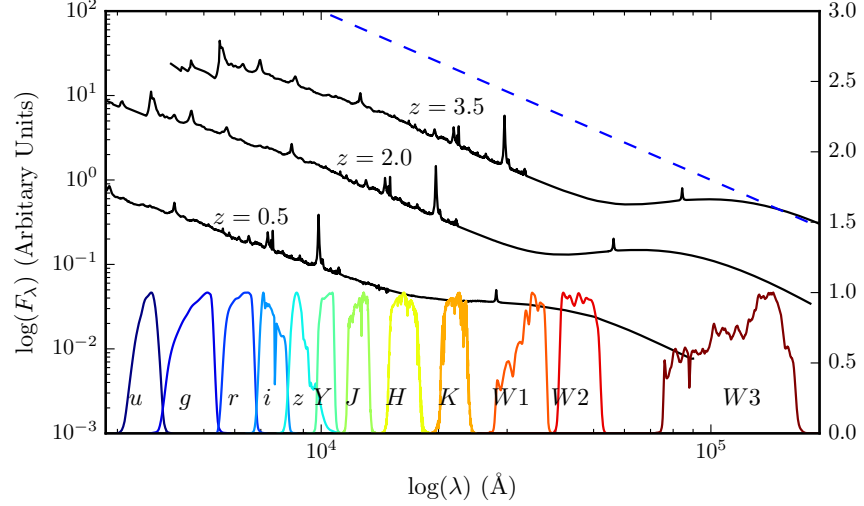


Figure 1.2: Model spectrum at three different redshifts (each arbitrarily scaled), and throughput functions for SDSS, UKIDSS and WISE band-passes (scaled so that the peak transmission is equal to one.) The dashed line indicates the slope of the AB magnitude system zero point.

in the rest frame of the quasar.

1.3 THE ‘STANDARD’ SED MODEL

We will begin by deriving a ‘standard’ SED model by constraining a single set of parameters with a large sample of $0.2 < z < 4$ quasars encompassing a range of luminosities, accretion rates etc. The free parameters in our model are the blue power-law slope, the red power-law slope, the power-law break wavelength, the blackbody temperature, the blackbody normalisation, the emission line equivalent width scaling, and the fractional contribution from the host galaxy to the total flux. The reddening $E(B-V)$ is fixed to zero, since a large fraction of SDSS quasars have very small amounts of dust reddening (Richards et al., 2003). For the host galaxy we use a Sb-type template derived by Mannucci et al., (2001). With some choice of initial parameters, we generate a set of model observed spectra at redshifts from $z = 0.25$ to $z = 3.75$ in intervals of $\Delta z = 0.1$. We then transform our set of model spectra into a set of model $ugrizYJHKW1W2$ SEDs

The throughput functions of the SDSS $ugriz$, UKIDSS $YJHK$ and WISE $W1W2W3$ band-passes are shown in Figure 1.2, along with our model AGN spectra at three different redshifts. The mean flux density in a band-pass P is given by

$$f_{\lambda}(P) = \frac{\int P(\lambda) f_{\lambda}(\lambda) \lambda d\lambda}{\int P(\lambda) \lambda d\lambda} \quad (1.25)$$

where $P(\lambda)$ is the dimensionless throughput function of the band-pass. The corresponding magnitude, $m_\lambda(P)$, is then

$$m_\lambda(P) = -2.5 \log(f_\lambda(P)) - m_0(P) \quad (1.26)$$

where $m_0(P)$ is the zero-point magnitude of band P . In the AB magnitude system, the zero-point flux per unit wavelength is

$$\frac{f_\lambda(\lambda)}{\text{erg cm}^{-2} \text{ s}^{-1} \text{ \AA}^{-1}} = 0.1087 \left(\frac{\lambda}{\text{\AA}} \right)^{-2}. \quad (1.27)$$

This is substituted into Equation 1.25 to give a zero-point mean flux density which is then converted into a corresponding magnitude.

The model SEDs are normalised such that the i magnitude of each model SED is 18.0 mag. This gives us an array of model magnitudes as a function of redshift and band-pass. We generate an equivalent data array by dividing our quasar sample into redshift bins from $z = 0.2$ to $z = 3.8$ with bin width $\Delta z = 0.1$. We normalise the individual quasar SEDs such that the observed i magnitude is equal to 18.0 mag, and then calculate a median SED in each redshift bin.

To fit the model to the data we minimise the sum of the squares of the differences between the elements in the model magnitude array and the elements in the data magnitude array. The minimisation is done using the ‘nelder-mead’ algorithm. Our SED model is valid only up to $\lambda \sim 3\mu\text{m}$ in the quasar rest frame (the approximate wavelength of the peak in hot dust emission); beyond this additional contributions to the total flux from cooler dust will become significant. This prevents us from using the two highest wavelength WISE bands in the fit. We also exclude the SDSS u and g band-passes from the fit at $z > 2.7$ and $z > 3.7$ respectively, where absorption in the Lyman α forest becomes large.

The best-fitting parameters from the fit are shown in Table 1.1. The colours ($u - g$, $g - r$, etc.) of the median SED, the individual quasars, and the best-fitting model are plotted as a function of redshift in Figs. 1.3 and 1.4. Most of the large variations that can be seen in the median colours of the quasars as a function of redshift are due to strong emission lines being redshifted in to and out of the bandpasses of the band-passes being used.

Re-do fit

1.4 DISCUSSION OF FIT

In Figure 1.5 we show the difference between the magnitudes from the best-fitting model and the median magnitudes from the sample. We have transformed the effective wavelengths of the band-passes to the rest frame of the quasars in each redshift bin, to give to the residuals as a function of rest-frame wavelength. We represent the

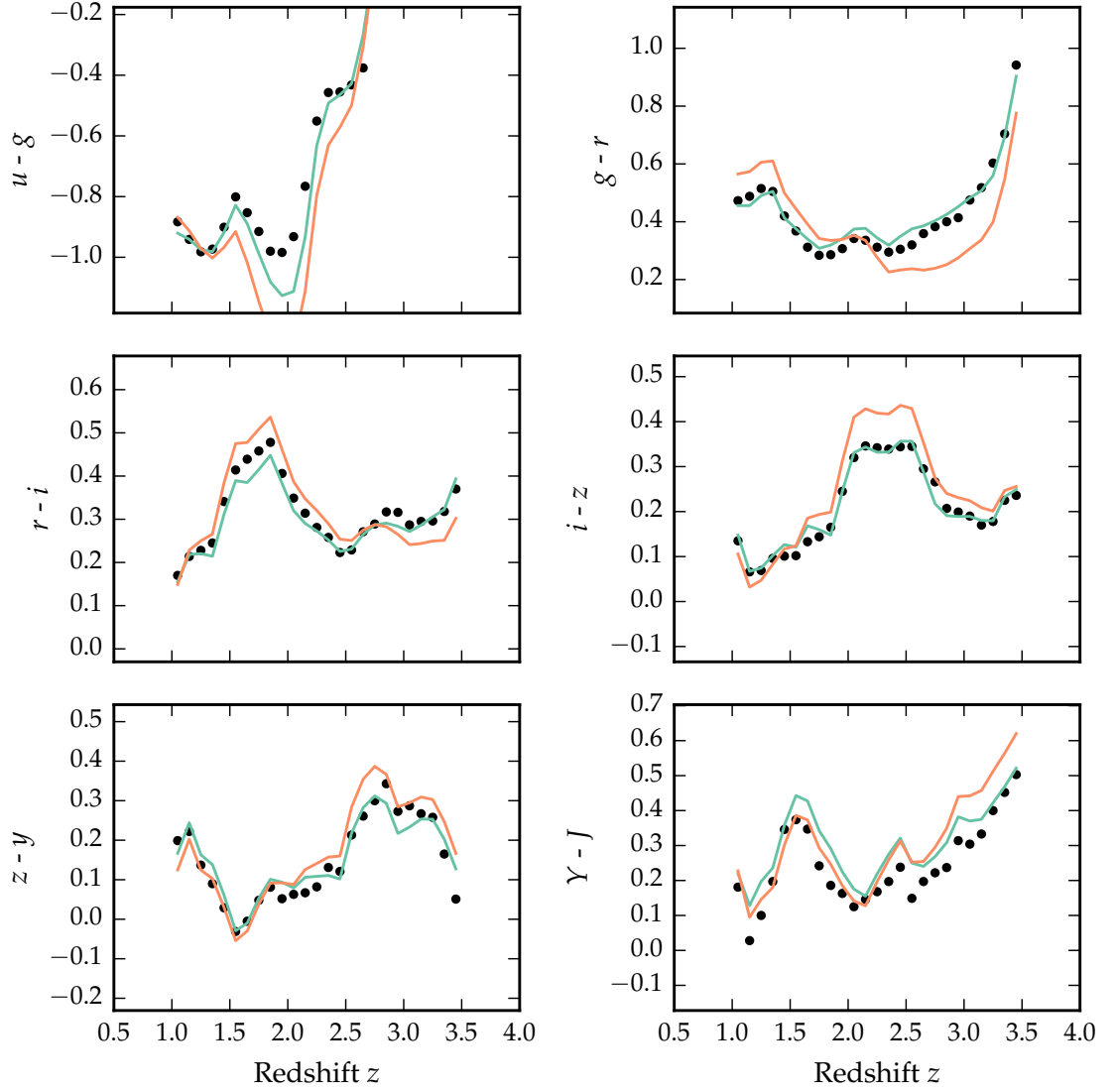


Figure 1.3: Colours of median SED (black circles), individual objects (grey points), best-fitting model (black line) as a function of redshift.

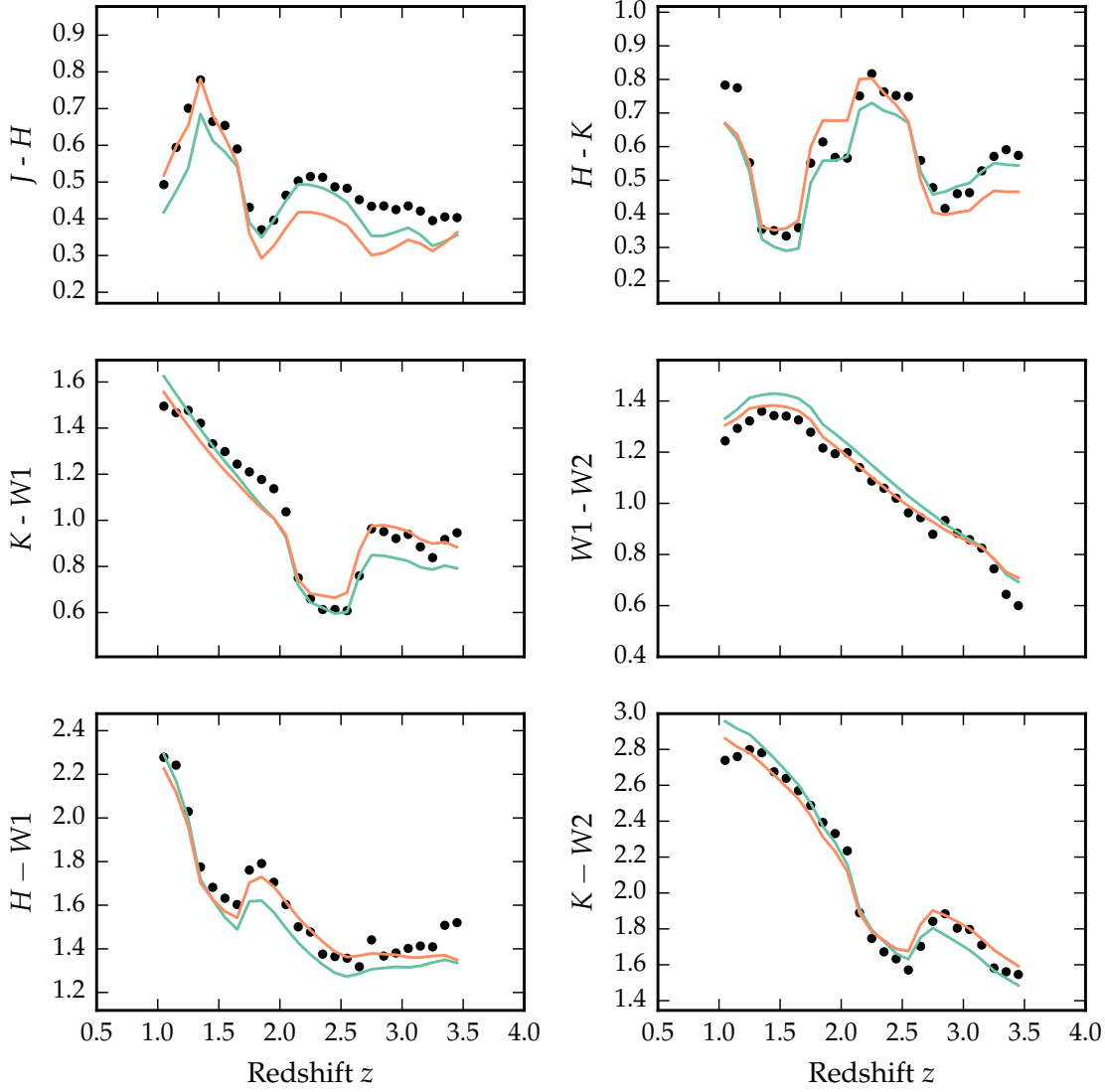


Figure 1.4: Colours of median SED (*black circles*), individual objects (*grey points*), best-fitting model (*black line*) as a function of redshift.

Parameter	Symbol	Before Correction	After Correction
Blue power-law index	α_{blue}	0.58	0.58
Red power-law index	α_{red}	-0.04	-0.05
Power-law break	λ_{break}	2945	2957
Blackbody temperature	T_{BB}	1216 K	1186 K
Blackbody normalisation	C_{BB}	0.22	0.21
Emission line scaling	C_{EL}	0.63	0.73
Galaxy fraction	η	0.29	0.28
E(B-V)	E(B-V)	0.00	0.00

Table 1.1: Best-fitting parameters from fit to DR7Q-matched sample. **Only give best-fit values after correction.**

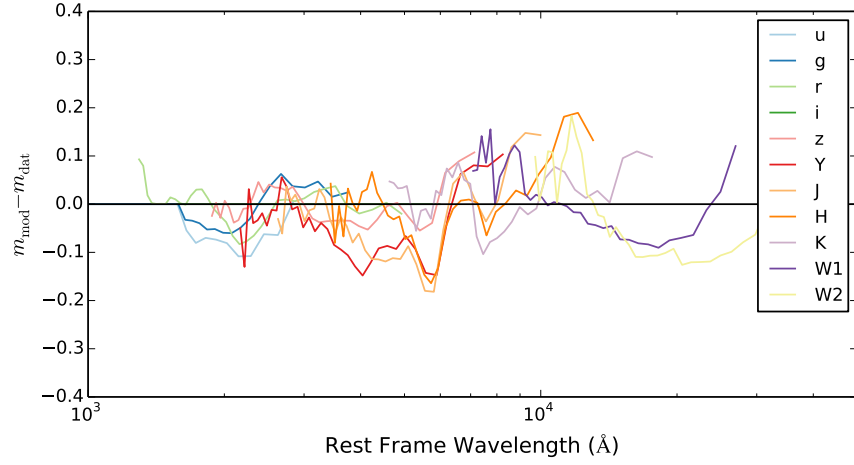


Figure 1.5: Residuals from fit to DR7Q-matched catalogue as a function of rest-frame wavelength.

residuals measured in each band-pass using a different coloured line. Differences between residuals from different band-passes at the same rest-frame wavelength could indicate redshift evolution of the typical quasar SED.

The residuals indicate that over a large redshift range the model does a fairly good at reproducing the median observed colours of the DR7Q-matched sample. Most discrepancies are at the < 0.1 mag level. It is remarkable that a single model is so effective; the properties of a typical quasar to not change significantly over a wide range of redshifts and luminosities. On the other hand, for the individual objects there is a significant scatter about the mean. In general, our goal is to use this intrinsic spread in SED properties in order to understand the diversity in physical quasar properties.

1.4.1 Flux Correction

1.5 HOT DUST

Including a black-body with $T \sim 1250\text{K}$, a simple parametric model matches the ugrizYJHKW1W2 (SDSS+UKIDSS+WISE) median colours of luminous quasars at redshifts $0.2 < z < 0.4$ extraordinarily well. The spread in the KW1W2 colours (Figure 1.8), probing the rest-frame $\sim 1\text{-}2$ micron region, is significant and strongly suggests presence of real variation in the "hot dust" temperature and luminosity among the quasars. Several other investigations have drawn attention to the rest-frame near-infrared SEDs, with populations of 'dust free' objects postulated (Hao et al., 2010; Hao et al., 2011; Jiang et al., 2010; Mor and Trakhtenbrot, 2011)

Reverberation measurements of nearby AGNs suggest that hot dust very close to the central source (few tens of light days; e.g. Minezaki et al., 2004; Suganuma et al., 2006). The hot dust signature could contain information about inner face of an obscuring torus structure and/or constrain the dust content of an accretion disk wind. Several studies have shown that the luminosity of the NIR excess emission correlates with that of the central engine with a slope close to unity e.g. Gallagher et al., 2007, suggesting that the dust is reprocessing radiation from the accretion disc.

Outflows may emerge from the outer region of the accretion disc or even the innermost region of the torus, in which the gas clouds are dusty and relatively cold. Indeed, there is observational evidence for dusty outflows close to the central engine (e.g. Bowler et al., 2014). The dust is heated by the central engine, and radiates in the near-infrared band. Wang et al., (2013), fitting the NIR emission with a single power-law, found that objects with strong outflow signatures (blue-shifted C IV) have more hot dust emission relative to the accretion disc emission in a large sample of $z \sim 2$ non-BAL quasars. It

*I have text on
empirical correction.
Re-do once I am
happy with SED
model*

could be that this correlation is induced by a third factor that simultaneously affects outflows and dust emission, for instance the inclination angle or metallicity. Alternatively the dust could be intrinsic to outflows and may have a non-trivial contribution to the outflow acceleration.

1.5.1 *Parameterising the hot dust emission*

We characterise the hot dust properties of our sample in terms of the temperature and luminosity of a blackbody. We choose to parameterise the luminosity in terms of the NIR to UV luminosity ratio (which is proportional to the covering factor of hot dust ($L_{\text{NIR}}/L_{\text{Bol}}$) used in other studies (Roseboom et al., 2013). The UV and NIR luminosity are calculated between 2000 and 9000Å and 1 and 3 μm respectively.

In Figure 1.6 we see that the two parameters are clearly correlated. For a lower temperature black-body the NIR to UV luminosity ratio is larger. Such a correlation is to be expected: as the black-body temperature is lowered, the peak shifts to longer-wavelengths (following Wien’s displacement law). Because of this degeneracy we need to be very careful to separate out real trends of $R_{\text{NIR/UV}}$ with other quasar properties from indirect trends resulting from a mutual dependence on T_{BB} .

Some previous studies (e.g. Wang et al., 2013; Zhang et al., 2014) have instead parameterised the near-IR emission using a power-law. We tested this parameterisation, and evaluated its effectiveness relative to using a black-body. The power-law is normalised at 9000Å, where its flux is set equal to the flux of the UV/optical model. The NIR power-law slope is fit between ~ 1 and $2.4\mu\text{m}$ (with the exact wavelength region being fit depending on the redshift of the quasar). We found large residuals in the best-fitting model which varied systematically as a function of $\lambda_{\text{eff}}/(1+z)$. This suggests that the power-law model is a poor fit to the shape of the near-IR emission. One needs to take care in looking at trends with luminosity given the observed-frame passband information on the rest-frame SED can produce some strong systematics with redshift, particularly if the SED-model is not a good fit to the actual SED. A similar conclusion was reached by Gallagher et al.

1.5.2 *Sample*

Our goal is to determine the temperature and abundance of the hot dust component in individual quasars. These properties will be measured by fitting a model to the SDSS-UKIDSS-WISE photometry. Constraining a $T \sim 1200\text{K}$ blackbody component in the SED model requires photometric data covering $\sim 1\text{--}3\mu\text{m}$ in the rest-frame of the quasar.

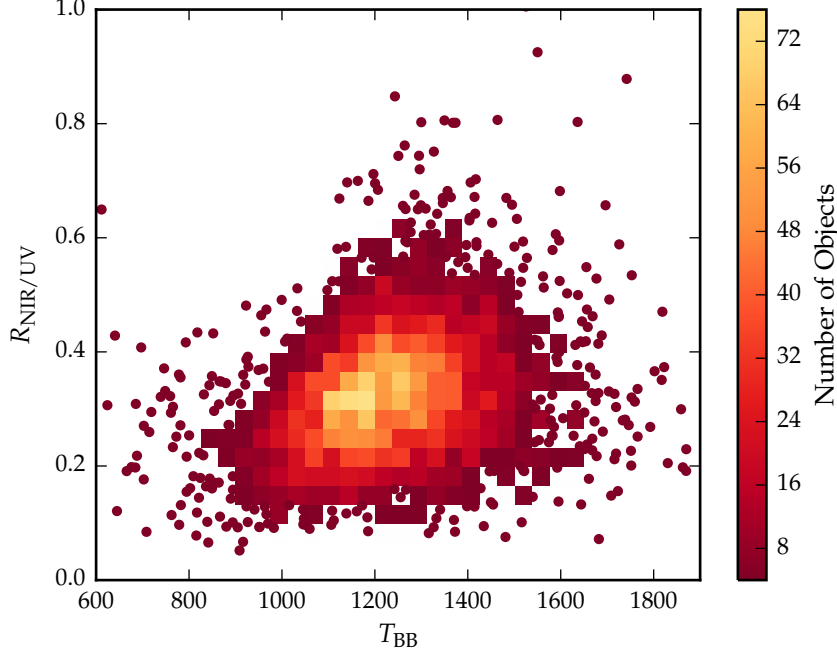


Figure 1.6: Ratio of NIR to UV luminosity ($R_{\text{NIR/UV}}$) against temperature (T_{BB}) for low- z sample. The density of points is shown in more dense regions of the space, and individual objects in less dense regions.

The observed-frame wavelength coverage of the available passbands limits the redshift range of the quasars which can be used. One does need to take care in looking at trends with luminosity given the observed-frame passband information on the rest-frame SED can produce some strong systematics with redshift, particularly if the SED-model is not a good fit to the actual SED. We consider only quasars at redshifts $z > 1$ where the relative host galaxy contribution to the SED is negligible. At redshifts $1 \lesssim z \lesssim 1.5$ the available ugrizYJHKW1W2 photometry provides good coverage of the rest-frame SED up to $\sim 2\mu\text{m}$. At $z \sim 1.5$ the W2 passband is shifted to $\sim 1.8\mu\text{m}$; at higher redshifts the wavelength coverage of the W2 band becomes much less than the peak wavelength of a $T \sim 1200\text{K}$ blackbody and experiments showed that such a component can not be adequately constrained by the available photometry. Quasars in the redshift interval $1.5 < z < 2$ are therefore excluded from our sample.

For the quasars at $z \sim 1$ the WISE W3 band is probing rest-frame wavelengths of $\sim 5 - 6\mu\text{m}$. This region of the SED is dominated by emission from cooler, more distant dust, which is not accounted for in our model. However, at redshifts $z \gtrsim 2$ the WISE W3 passband probes sufficiently short wavelengths to be useful in constraining the shape of the hot blackbody component. Therefore for quasars at redshifts $z > 2$ we again have sufficient constraints from the

ugrizYJHKW1W2W3 photometry to determine the temperature and normalisation of the blackbody component. There are few objects in our sample with redshifts $z > 2.7$, and so we set this as an upper limit on the redshift of our sample. Because of these constraints, our sample is divided into two parts: one at low redshifts ($1 < z < 1.5$) and the other at higher redshifts ($2 < z < 2.7$).

We include only quasars with observed magnitudes brighter than 19.1 in the *i* band-pass, i.e. the quasars selected by the main SDSS quasar selection algorithm (70,214 quasars). Cross-matching (with a $2''$ radius and picking only the nearest neighbour) the SDSS DR7Q catalogue with the ULAS catalogue, which covers only $\sim 38\%$ of the SDSS foot-print, resulted in 37,886 matches. Of these 36,628 have been detected in one or more of the WISE band-passes. We exclude quasars flagged as broad-absorption line quasars from the sample (leaving 35,272 quasars). We impose a lower-limit signal-to-noise ratio (S/N) > 5 magnitudes in the *K*, *W1* and *W2* band-passes for the low-*z* sample and $S/N > 5$ in the *W1*, *W2*, and *W3* band-passes for the high-*z* sample to ensure reliable photometry. This gives us 5,910 quasars in our low-*z* sample and 1,989 quasars in our high-*z* sample.

We will hold most parameters fixed, and vary only those we are interested in, i.e. the blackbody parameters which parameterise the NIR emission. Therefore we need to define a sub-sample of objects which we know are well fit by our standard SED model in the UV/optical region. This means excluding objects with extreme emission line equivalent widths or significant dust extinction. We use the *i* – *K* colours of the quasars as a measure of the overall colour of the quasars as it provides the longest baseline in wavelength without being affected by absorption in the Ly α forest at high redshifts. We discarded from our sample quasars with *i* – *K* colors redder than our standard model with dust reddening $E(B-V) = 0.075$ and bluer than $E(B-V) = -0.075$ (Figure 1.7). Following this cut we are left with 4,615 quasars in our low-*z* sample and 1,692 quasars in our high-*z* sample.

1.5.3 Diversity in hot dust properties

In Figure 1.8 we plot the *W1* – *W2* colors of the DR7Q-matched sample as a function of redshift at $z < 3$. In this redshift range the *W1* and *W2* band-passes are probing the $1.2 - 2.8\mu\text{m}$ and $1.6 - 3.8\mu\text{m}$ region of the rest frame SED respectively. For reference, the peak wavelength is at $2.4\mu\text{m}$ for a black-body radiating at 1200K (close to the sublimation temperature of dust grains). At any given redshift we see a ~ 0.5 mag dispersion in the *W1* – *W2* colors.

On the same axes in the Figure we have plotted the *W1* – *W2* colors derived from our SED model with a fixed blackbody temperature (1216K) and a ratio of NIR to UV luminosity ranging from 0.0 to 1.0, with the other model parameters held constant. We conclude that

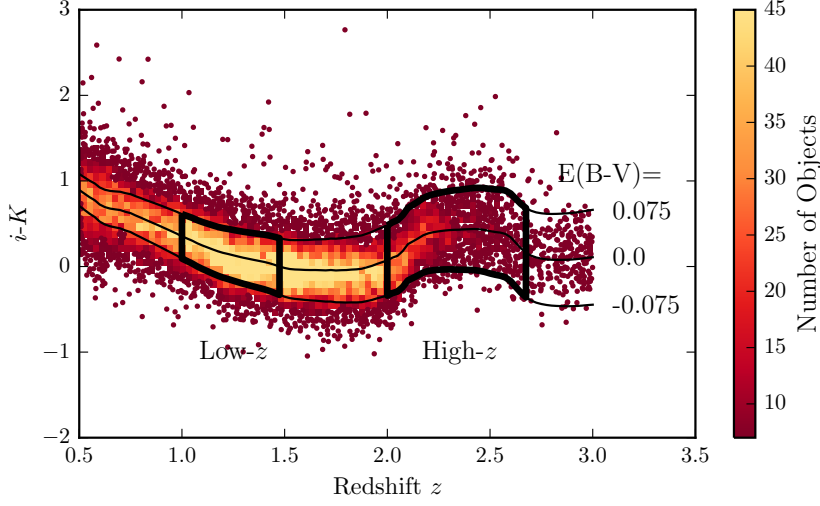


Figure 1.7: $i-K$ vs z . Demonstrates how sample was defined. The grey points show, as a function of redshift, the $i-K$ colours of all DR7Q quasars which are not classified as broad-absorption line quasars by Shen et al. and i magnitude > 19.1 . The black line shows the $i-K$ colour of our standard, unreddened SED model as a function of redshift. The red and blue lines show the $i-K$ colours of our SED model with dust reddening $E(B-V) = 0.075$ and $E(B-V) = -0.075$ respectively. A significant amount of this reddening can be attributed to intrinsic variations in the UV power-law slopes of the individual quasars, which is why we allow a negative reddening. However, there is a clear ‘red tail’ to the colour distribution which can be explained by dust reddening at the redshift of the quasar. We defined two samples, at low ($0.5 < z < 1.5$) and high ($2 < z < 2.7$) redshift, which are shown in the figure.

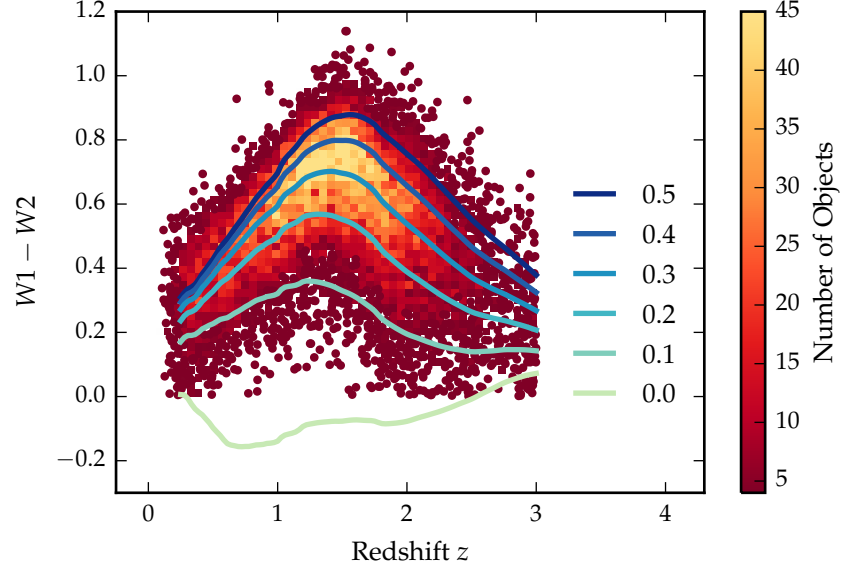


Figure 1.8: $W1 - W2$ colours of DR7 sample as a function of redshift. Above a certain density threshold points are represented by a density plot. On top we plot the colours of our standard SED model, with a fixed temperature and a varying NIR ($1 - 3 \mu\text{m}$) to UV ratio.

even with the sample restricted to be fairly uniform in its UV/optical properties, we still get an interesting spread in $W1-W2$ colors, which we can use to learn about the diversity of NIR properties in our sample. In the rest of this chapter we will characterise the hot dust properties of our sample, and test its relation to quasar properties such as luminosity, black-hole mass and normalised accretion rate, and outflow-properties.

In Figure 1.6 we show that there is quite a range of temperature and normalisation present in our sample. However, we need to check how much of this is due simply to uncertainties in the fits stemming from uncertainties in the photometry. In order to achieve this we took our standard SED model with a single temperature and normalisation black-body component, and generated 200 mock SEDs with a brightness distribution similar to that of our real sample. We estimated the mean uncertainty of the magnitudes in the K, $W1$, and $W2$ band-passes as a function of apparent brightness. We then sampled the K, $W1$, and $W2$ magnitudes from Gaussian distributions, with a mean equal to the magnitude of the model SED, and the width equal to the mean uncertainty at the appropriate brightness. Finally, we fit these mock SEDs using our standard fitting procedure. The results are shown in the Figure below, on top of the results from our real sample (shown as grey contours). We can see that uncertainty in the photometry introduces a significant scatter to the temperature,

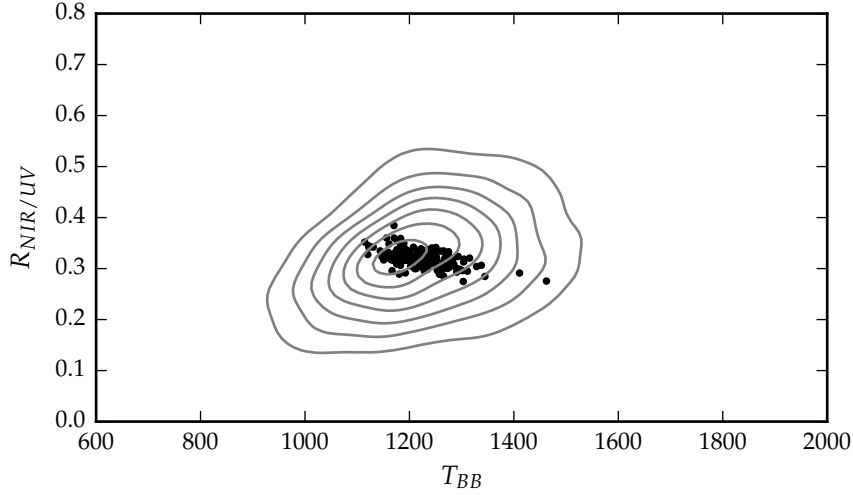


Figure 1.9: Ratio of NIR to UV luminosity ($R_{\text{NIR/UV}}$) against temperature (T_{BB}). The grey contours show equally-spaced lines of constant probability density generated using a Gaussian kernel-density estimator on our data sample. The black points are for our mock data.

but that this scatter is less than the intrinsic scatter in the data. This demonstrates that there is a real distribution of hot dust temperatures and luminosities in our sample.

1.6 FITTING PROCEDURE

We will fit a model to the individual quasar SEDs, allowing the temperature and normalisation of the black body component to vary. The model spectrum is redshifted to the redshift of the quasar being fit and is then multiplied by the `ugrizYJHMW1W2W3` throughput functions and normalised appropriately to give AB magnitudes. To fit the model to the data we minimise the sum of the squares of the differences between the elements in the model magnitude array and the elements in the data magnitude array. To avoid significant absorption in the Lyman- α forest at high- z , we restrict our fitting to wavelengths greater than 2000Å; when the effective wavelength of a band-pass falls below this limit the band-pass is excluded from the fit. The minimisation is done using the 'nelder-mead' method, as implemented in the `minimize` function from the Python module `scipy`.

*2000Å is quite large
given the
Lyman-alpha forest
impacts from 1216Å.*

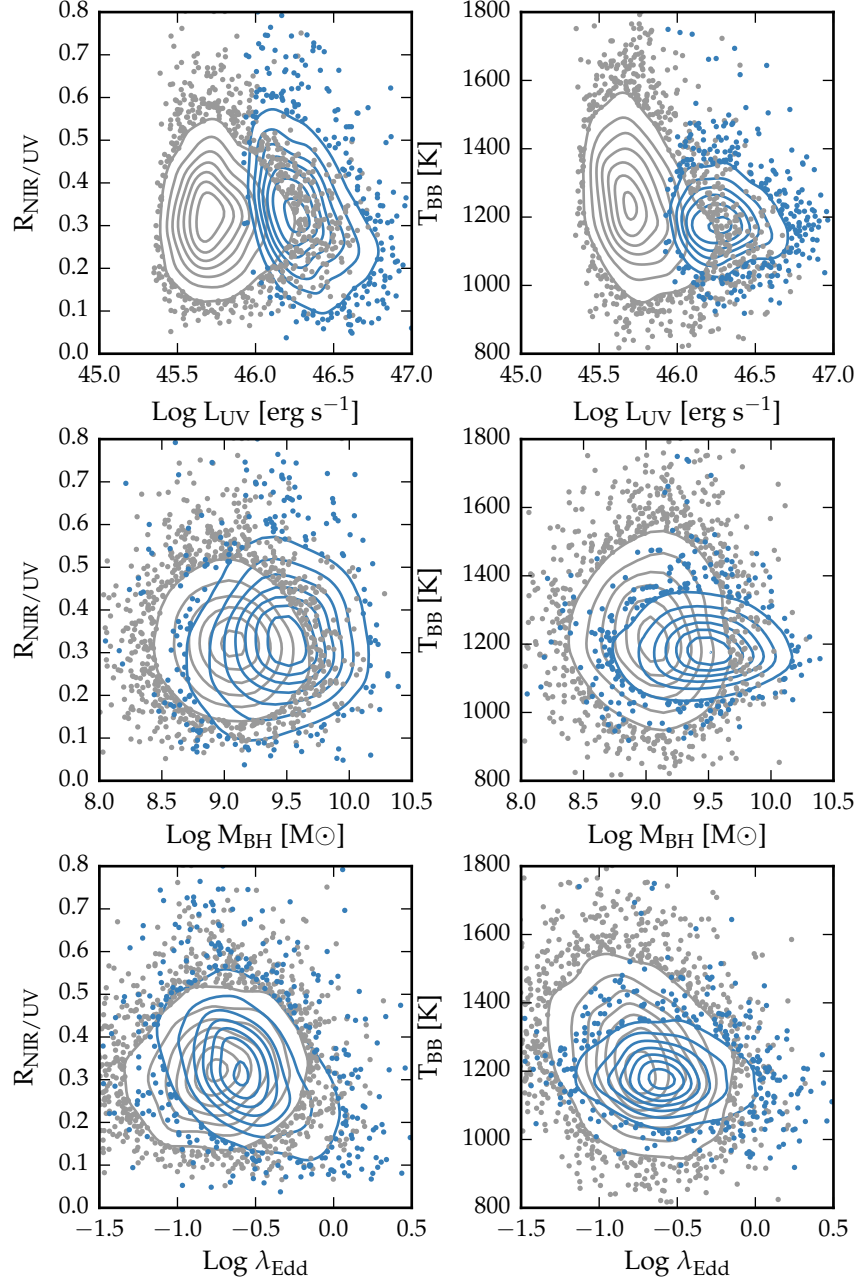


Figure 1.10: Best-fit black-body temperature against UV luminosity (left), black-hole mass (center) and Eddington ratio (right) for $1 < z < 1.5$ sample (black) and $2 < z < 2.7$ sample (black). In region of high-density we represent the density with contours generated using a Gaussian kernel density estimation. **Needs re-making with new BH masses.**

1.7 RESULTS

1.7.1 Correlations with quasar properties

We now look for correlations between the properties of the black-bodies we have fitted to the hot dust emission and other properties of the quasar such as redshift, black-hole mass, and normalised accretion rate (Eddington ratio).

Calculate new BH masses and redo this section.

1.7.2 Spectral properties

In the dusty wind model - first proposed by Konigl and Kartje, (1994) and later developed by, amongst others, Everett, (2005), Elitzur and Shlosman, (2006), Keating et al., (2012) - the ‘torus’ is the dusty part of a magneto-hydrodynamic wind beyond the dust sublimation radius. The MHD wind is roughly polar, and so the hot dust forms a vertical ‘wall’ around the accretion disk. UV photons from the accretion disk accelerate the wind via radiation line driving. That flattens the geometry of the wind and exposes more surface area that is viewable on a relatively face-on line of sight. The radiation pressure is increased at higher luminosities and/or accretion rates. This can flatten the geometry of the wind, thereby increasing the range of angles for which the inner edge of the dusty wind - where dust is at its sublimation temperature - can be observed. A direct prediction is therefore that the in a quasars with high accretion rates and strong outflows, the emission from hot dust should be enhanced.

1.7.2.1 Low- z

The $z < 0.8$ SDSS spectrum composite comparison for the small and large β_{NIR} sub-samples is a very direct illustration of the Boroson and Green, (1992) Eigenvector 1 describing the spectral variation in the optical spectra of quasars; as Fe II EW increases the [O III] EW decreases. Hot dust emission increases with Fe II EW (Shen and Ho, 2014). We also note that the amount of hot dust correlates with the Si III/C III] emission ratios. The Si III/C III] ratio is generally considered to be a good indicator of density and is one of the primary EV1 correlates. The relative flux ratio of Si III to C III] increases when C IV is more blue-shifted (Richards et al., 2011). The Mg II emission line has exactly the same profile/shape for the two samples (apparent changes in Mg II seen in Fig. 1.11 are the result of changes in Fe II at wavelengths just shortward of the line). Finally, we note that objects with more hot dust are slightly redder.

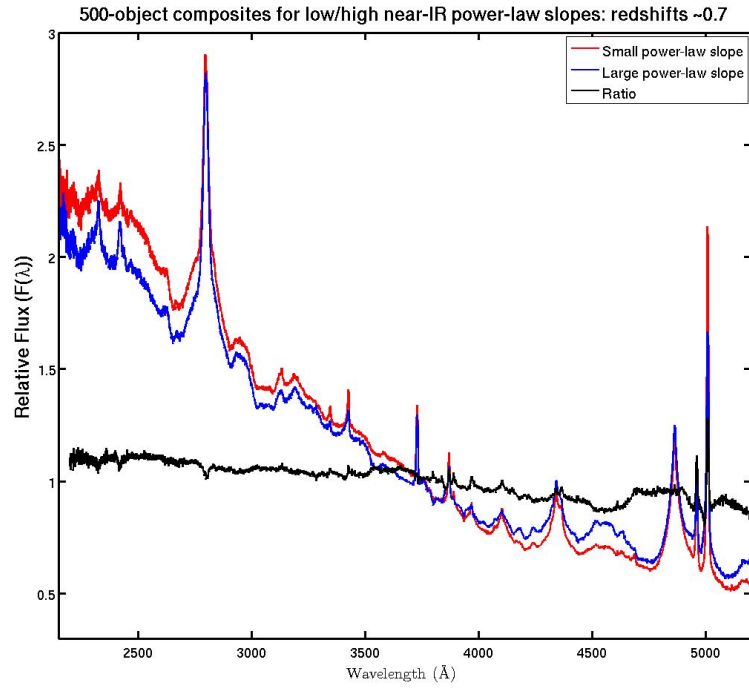


Figure 1.11: Composite SDSS spectra for objects at $z \sim 0.7$. We have divided sample into objects with objects best-fit by small (red line) and large (red line) values of β . **Change this to select by $R_{\text{NIR/UV}} / T_{\text{BB}}$. Label prominent emission lines.**

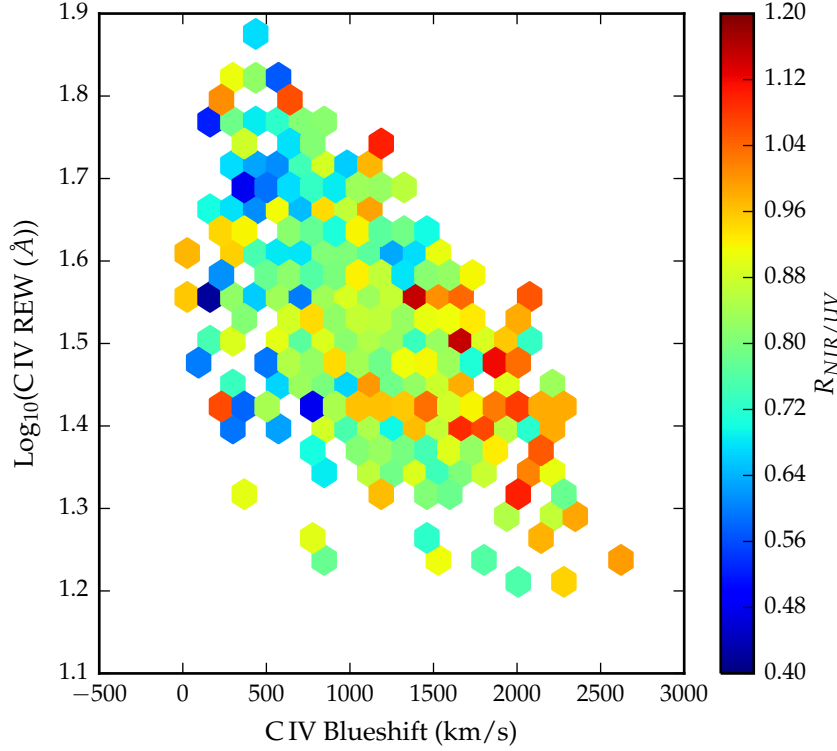


Figure 1.12: Rest-frame equivalent width and blueshift of the C iv line for 7,115 SDSS DR7 quasars. The colours of the hexagons denote the median hot dust ($T \simeq 1200$ K) abundance for all quasars at a given equivalent width and blueshift. Quasars with the most extreme outflow signatures are predominantly hot-dust rich. Only bins containing a minimum of two objects are plotted.

1.7.2.2 High- z

In Fig. 1.12 we show how the ratio of NIR to UV luminosity depends on the blueshift and rest-frame equivalent width of the C iv line. C iv blueshifts are calculated as in Section XX. We see that the NIR to UV luminosity ratio is strongly correlated with the blue-shift of the C iv emission line. A similar trend was noted by Wang et al., (2013). Interestingly, we note strong similarities to the object subsets selected according to their C iv-emission properties in Richards et al., (2011) (see Figures 11 & 12). We note that the correlation between the hot dust and the C iv emission properties will lead to apparent correlations between the host dust and the BH mass.

1.7.3 BALs and radio-loud/radio-quiet

In the spectra of about 20% of all quasars we observe broad (> 2000 km/s) blue-shifted absorption troughs which are associated with quasar-driven out-flowing gas. BAL quasars in general have redder

Need to re-do this and understand why beta-related trend is apparently stronger than with the blackbody parameters.

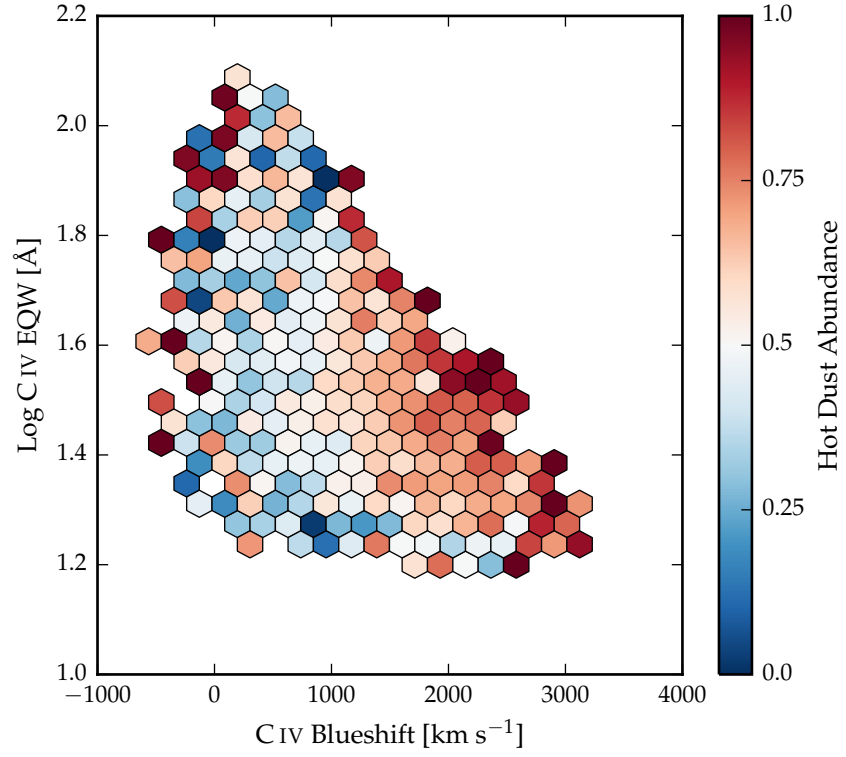


Figure 1.13

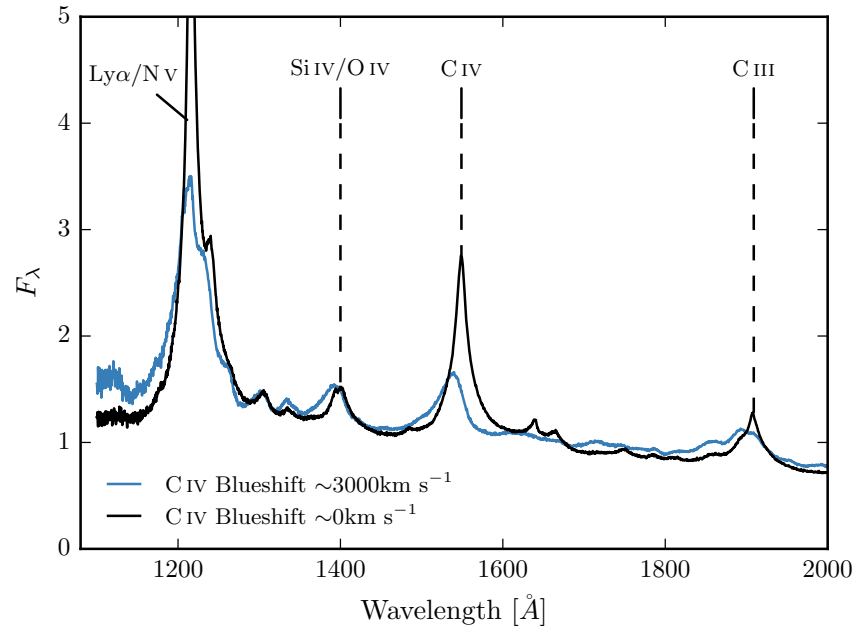


Figure 1.14

UV continua than non-BAL quasars, which is interpreted as the result of dust extinction. BAL quasars, on average, also have higher Eddington ratios and luminosities than non-BAL quasars.

We defined a sample of BAL quasars using the same method we used to define our sample of non-BAL quasars. At $1 < z < 1.5$ there are very few BAL quasars in our sample. In the $2 < z < 2.7$ redshift region we have 394 HiBAL quasars (the wavelength coverage of the SDSS spectra are not sensitive to LoBALs at these redshifts). Since BAL quasars are expected to suffer more from extinction due to dust, we have allowed $E(B-V)$ to vary for the BAL quasar sample.

We find that the black-body temperature distributions are consistent (median T_{BB} for both samples = 1180K), but the ratio of NIR to UV emission is higher in BALs ($R_{NIR/UV} = 0.92$ and 0.83 for BAL and non-BAL quasar sample respectively). This is qualitatively consistent with the results of Zhang et al., (2014).

It is well known that the blueshift of the C IV emission line in radio-quiet AGNs is, on average, stronger than in radio-loud AGNs (Marziani et al. 1996; Sulentic et al. 2000a; Richards et al. 2002, 2011). Statistically at least, the "radio-loud" objects are thought to have high black-hole masses and there is some form of radio-mode feedback (jet related) which is very different from the much more common (almost certainly wider opening-angle) outflow objects with large C IV blueshifts.

So we find BALs have more hot dust, radio-loud have less. This is perfectly consistent with what we know about the positions of radio-loud objects and BALs in the C IV parameter space distribution (Richards et al., 2011).

Need to justify our use of model which has been optimised to fit colours of non-BAL quasars, when we know that BALs are typically redder.

What catalogue did we use to define quasar sample?

1.8 OTHER WORKS

Roseboom et al., (2013) studied a similar sample of luminous type 1 quasars. They, like us, modelled the NIR emission using a black-body and modelled the emission at longer wavelengths using a clumpy torus model. They find that while $L_{1-5\mu m}/L_{IR}$ appears relatively insensitive to L_{bol} and L_{IR} , a strong correlation appears between $L_{1-5\mu m}/L_{IR}$ and L_{IR}/L_{bol} (i.e. the dust covering factor). As the covering factor decreases, the maximum inclination at which a type 1 quasar would be seen increases. An increase in the inclination will mean direct sight lines to more of the inner wall of obscuring material closest to the accretion disc.

Mor and Trakhtenbrot, (2011) also looked at the hot dust properties of a sample of $0.75 < z < 2$ quasars, with photometry from SDSS and WISE. They modelled the NIR emission with hot clouds of pure graphite dust. They reported an anti-correlation between the covering factor of hot dust clouds and the quasar bolometric luminosity. Like us, they neglect cooler dust components which will dominate

the SED at longer wavelengths. As we have discovered (see Figure residual plot), the missing flux decreases with redshift because we observe shorter rest-frame wavelengths when the observed spectrum is redshifted to a greater degree. This will induce an anti-correlation between the luminosity of the hot dust component and the luminosity of the quasar (which is correlated with redshift). At $z=0.75$, the W_3 band-pass (the longest in their fits) is sensitive to flux from $6.9\mu\text{m}$; at this wavelength we expect the contribution from cooler dust to dominate over the hot dust. It is possible that this effect could explain the tension with our own result that $R_{\text{NIR/UV}}$ does not depend on the quasar luminosity in our low- z sample.

Shen and Ho, (2014) quantify the relative torus emission using the $r - W_1$ colour for a sample of $0.4 < z < 0.8$ SDSS quasars. At these redshifts W_1 is observing between 1.9 and 2.4 microns in the rest-frame of the quasar, which suggests that they are sensitive to the same component of hot dust which we are investigating. They observe a mild trend of decreasing relative torus emission as the quasar luminosity increases. We note that their use of the $r - W_1$ at much higher redshifts may be problematic, as the W_1 flux will be increasingly dominated by direct emission from the accretion disc.

Gallagher et al., (2007) undertook a similar investigation for a much smaller sample of 234 radio-quiet quasars.

1.8.1 Eddington ratio

Wang et al., Zhang et al., and Mor & Trakhtenbrot find no significant dependence of the amount of hot dust on the Eddington ratio.

Shen & Ho find that torus emission is enhanced in quasars with larger R_{FeII} . They show how $\text{EW}(\text{OIII})$ and other high-ionisation lines (and to a lesser extent low-ionisation lines like MgII) anti correlate with R_{FeII} . The enhancement of torus emission relative to accretion disc emission at the high- R_{FeII} end of EV_1 may be caused by more efficient disc winds that facilitate the formation of a dusty torus. From our $z \sim 0.8$ composite SDSS spectra, we observed that objects with large NIR to UV luminosity ratios on average have stronger FeII emission.